Dispersive Dark Excitons in van der Waals Ferromagnet CrI$_3$

W. He[1,*,†] J. Sears,[1] F. Barantani,[2] T. Kim,[3] J. W. Villanova,[4] T. Berlijn,[4] M. Lajer,[1] M. A. McGuire,[5] J. Pelliciari,[3] V. Bisogni,[3] S. Johnston,[6,7] E. Baldini,[2] M. Mitrano,[8] and M. P. M. Dean[1,‡]

[1]*Department of Condensed Matter Physics and Materials Science,*
Brookhaven National Laboratory, Upton, New York 11973, USA
[2]*Department of Physics, The University of Texas at Austin, Austin, Texas 78712, USA*
[3]*National Synchrotron Light Source II, Brookhaven National Laboratory, Upton, New York 11973, USA*
[4]*Center for Nanophase Materials Sciences,*
Oak Ridge National Laboratory, Oak Ridge, Tennessee 37831, USA
[5]*Materials Science and Technology Division, Oak Ridge National Laboratory,*
1 Bethel Valley Road, Oak Ridge, Tennessee 37831, USA
[6]*Department of Physics and Astronomy, The University of Tennessee, Knoxville, Tennessee 37966, USA*
[7]*Institute for Advanced Materials and Manufacturing,*
The University of Tennessee, Knoxville, Tennessee 37996, USA
[8]*Department of Physics, Harvard University, Cambridge, Massachusetts 02138, USA*

Spin-flip dark excitons are optical-dipole-forbidden quasiparticles with remarkable potential in optoelectronics, especially when they are realized within cleavable van der Waals materials. Despite this potential, dark excitons have not yet been definitively identified in ferromagnetic van der Waals materials. Here, we report two dark excitons in a model ferromagnetic material CrI$_3$ using high-resolution resonant inelastic x-ray scattering and show that they feature narrower linewidths compared to the bright excitons previously reported in this material. These excitons are shown to have spin-flip character, to disperse as a function of momentum, and to change through the ferromagnetic transition temperature. Given the versatility of van der Waals materials, these excitons hold promise for new types of magneto-optical functionality.

I. INTRODUCTION

Excitons play a key role in determining the optical properties of solids, and their strong light-matter coupling paves the way for exploring new aspects of many-body physics [1]. Dark excitons are particularly interesting, because they involve optical-dipole-forbidden transitions [2]. For this reason, they have reduced rates of radiative recombination and enhanced lifetimes, and in many cases they can be sensitively controlled by external means, such as a magnetic field [3]. These properties endow them with great potential in quantum information storage and communication [4].

Early studies of dark excitons began in the 1990s with quantum dots [5], followed by research on organic materials [6] and later expanded to transition-metal dichalcogenides [7]. The recent discovery of magnetic van der Waals (vdW) materials provides a new platform for studying excitons [8–12], and fascinating interactions between magnetism and excitons have been observed in several antiferromagnetic systems [13–17]. Understanding the electronic structure of these excitons and their interactions with magnetism is not only interesting from a fundamental point of view, but it may also offer new types of magneto-optical functionality such as optical readout of magnetic states or quantum sensors [18]. CrI$_3$ provides an opportunity to study excitons in a ferromagnetic (FM) vdW material even down to the monolayer limit [19,20]. Optical studies have revealed several bright excitons around 1.50, 1.85, and 2.2 eV in this material alongside several other optical features [20–23]; however, dark excitons have not been definitively identified.

Resonant inelastic x-ray scattering (RIXS) is directly sensitive to optically forbidden excitations and has recently

*Present address: Stanford Institute for Materials and Energy Sciences, SLAC National Accelerator Laboratory, Menlo Park, California 94025, USA.
†Contact author: weihe@stanford.edu
‡Contact author: mdean@bnl.gov

emerged as a powerful probe of excitons and their interactions with magnetism, in several magnetic vdW materials [13,15–17,24,25]. In this paper, we use Cr L_3-edge RIXS to identify two dark excitons near 1.7 eV in CrI$_3$. Both dark excitons are much sharper than other bright excitons and disperse with a bandwidth (approximately 10 meV) similar to the energy scale of magnetic exchange interactions in this material. Together with the change of their intensities across the FM ordering temperature T_c, our experimental findings suggest an intimate relationship between CrI$_3$'s dark excitons and its magnetism. The electronic character of the dark excitons is borne out by our exact diagonalization (ED) calculations, which reveal that these excitons are spin-flip transitions in nature and are predominantly governed by Hund's coupling.

II. METHODS

Bulk single crystals of CrI$_3$ were synthesized by reacting the elements together in an evacuated fused silica ampoule [26]. CrI$_3$ undergoes a structural phase transition between the high-temperature monoclinic structure (space group $C2/m$, No. 12) and the low-temperature rhombohedral structure (space group $R\bar{3}$, No. 148) over a broad temperature range (100–220 K) upon thermal cycling. The temperature of the sample was kept at $T = 30$ K, deep into the FM phase of the material, unless otherwise specified. We use the rhombohedral unit cell notation with lattice parameters $a = b = 6.867$ Å, $c = 19.807$ Å, and $\gamma = 120°$ throughout the manuscript and index reciprocal space in terms of scattering vector $Q = (H, K, L)$ in reciprocal lattice units (r.l.u.).

To avoid sample degradation in air, we mounted the sample on a copper sample holder in a glove box, cleaved with Scotch tape in N$_2$ atmosphere (approximately 3% relative humidity level) to expose a fresh surface, and directly transferred the cleaved sample into the RIXS sample chamber. The surface normal of the sample is parallel to the c axis. The in-plane orientation was determined by checking the residue on the Scotch tape with a laboratory single-crystal x-ray diffractometer.

Cr L_3-edge RIXS measurements were performed at the SIX 2-ID beamline of the National Synchrotron Light Source II. Data were taken with linear horizontal (π) polarization in the ($H0L$) scattering plane unless otherwise specified. The spectrometer was operated with a high-energy resolution of 30.5 meV full width at half maximum (FWHM) (the exit slit size was 30 μm). Since the interlayer coupling in CrI$_3$ is weak, we fixed the scattering angle at $2\Theta = 150°$ and express Q in terms of the projected in-plane component of the momentum H. An angle-dependent self-absorption correction [27] was applied to the RIXS spectra, which, however, does not affect exciton energies or relative intensity changes at fixed Q. The x-ray absorption spectroscopy (XAS) spectra were taken using the partial fluorescence yield mode with the RIXS detector, which

covers energy loss up to approximately 11 eV. The exit slit size was much larger (300 μm) for the XAS measurements to increase the flux.

III. IDENTIFICATION OF DARK EXCITONS

Figure 1(a) shows Cr L_3-edge RIXS spectra of CrI$_3$ as a function of incident x-ray energy. Peaks below 2.5 eV energy loss are mainly local transitions within the Cr $3d$
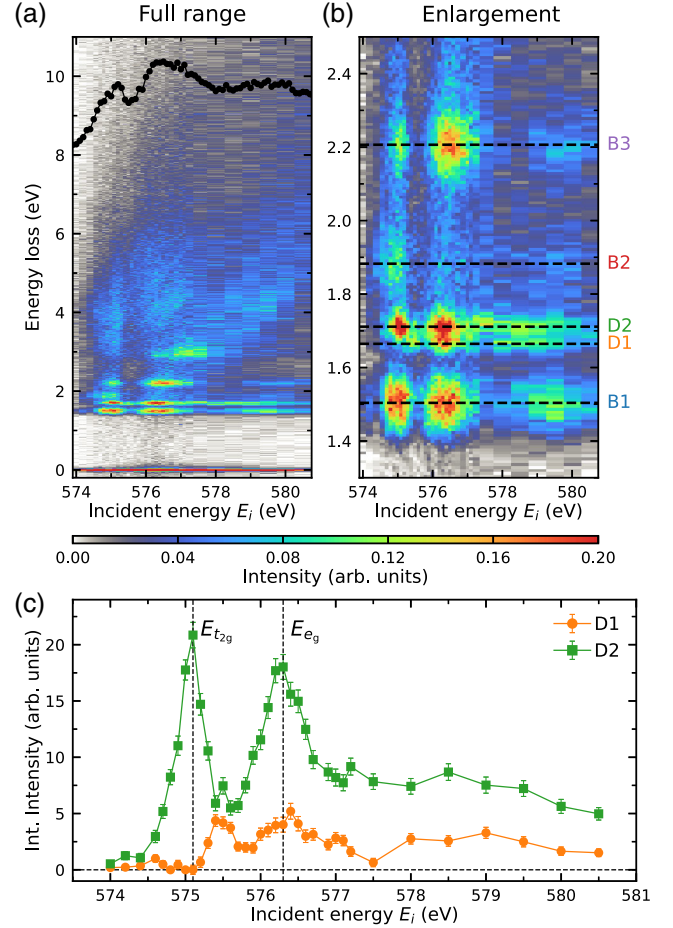

FIG. 1. Resonance behavior of dark excitons. (a) Cr L_3-edge RIXS incident energy map taken at $T = 30$ K with π-polarized x-rays incident on the sample at $\theta = 14.5°$ and scattered to $2\Theta = 150°$ in the ($H0L$) scattering plane, corresponding to $H = -0.46$ r.l.u. The overlaid black curve on the top is the XAS spectrum taken at the same conditions (including x-ray polarization, experimental geometry, and temperature). (b) Enlargement of the exciton resonances. Horizontal dashed lines are fitted exciton energies. Two peaks near 1.7 eV are identified as the dark excitons and denoted as D1 and D2. The other three peaks are bright excitons previously observed in optical measurements [20–23] and, therefore, denoted as B1–B3. (c) The fitted integrated intensities of the two dark excitons as a function of incident photon energy E_i through the $E_{t_{2g}}$ and E_{e_g} resonances. D1 resonates at E_{e_g}, whereas D2 resonates at E_{e_g} and $E_{t_{2g}}$. As shown in Supplemental Material Sec. S1, these effects show minimal dichroism [32].

orbital manifold, while broad features at higher energy can be ascribed to charge transfer processes that heavily involve ligand orbitals and x-ray fluorescence arising from more extended states [28]. In the 1–3 eV energy window depicted in Fig. 1(b), three peaks, located at 1.50, 1.88, and 2.21 eV, match the exciton energies previously reported in optical experiments [20–23], so we denote them as bright excitons B1–B3. More excitingly, two additional features are observed at 1.66 and 1.71 eV, which were not seen in prior RIXS measurements due to their lower resolution (180/350 meV compared to 30.5 meV used here [29,30]). These modes have not yet been definitively identified in optical spectra, so, following standard terminology in optics, we refer to these as dark excitons and denote them as D1 and D2. We note that there are no additional features at energies below B1, contrary to an earlier prediction that the lowest-energy dark excitons should exist around 0.9 eV [31].

Figure 1(b) exhibits two prominent resonances at $E_i =$ 575.1 and 576.3 eV. Although there is strong $t_{2g} - e_g$ mixing in CrI$_3$, these two resonances correspond to more t_{2g}-like and more e_g-like orbital manifolds, respectively, as shown in Supplemental Fig. S16 [32]. We, therefore, label them as $E_{t_{2g}}$ and E_{e_g} resonances hereafter. As shown in Fig. 1(c), D2 resonates with t_{2g} and e_g intermediate states, but D1 resonates only at the e_g condition. An additional small resonance is present around 575.5 eV, which is

generated by the exchange part of the core-valence Coulomb interaction on the Cr site. We use the excitons' energy and angular dependence to identify their electronic character later in this article.

IV. DARK EXCITON DISPERSION

Having identified the existence of dark excitons in CrI$_3$, we explore their propagation by mapping out their in-plane dispersion at the two resonant energies $E_{t_{2g}}$ and E_{e_g}, as presented in Figs. 2(a) and 2(b). Intriguingly, both excitons D1 and D2 exhibit a small dispersion but with opposite trends. We cofit the spectra at the two different resonances, as described in Supplemental Material Sec. S3 [32] and shown in Fig. 2(c). The fitted exciton energies in Figs. 2(d) and 2(e) confirm the presence of dispersion with similar bandwidths of approximately 10 meV. Such bandwidths are comparable to the energy scale of the magnon dispersion [33], hinting at the involvement of exciton-magnon interactions when these dark excitons propagate in the lattice. The widths of the two dark excitons are dramatically sharper than those of other bright excitons, especially D1, which is almost resolution limited and about 10 times narrower than the bright excitons [see Fig. 2(b)]. The three bright excitons do not exhibit any detectable dispersion (see Supplemental Fig. S9 [32]), likely due to their broader linewidths.
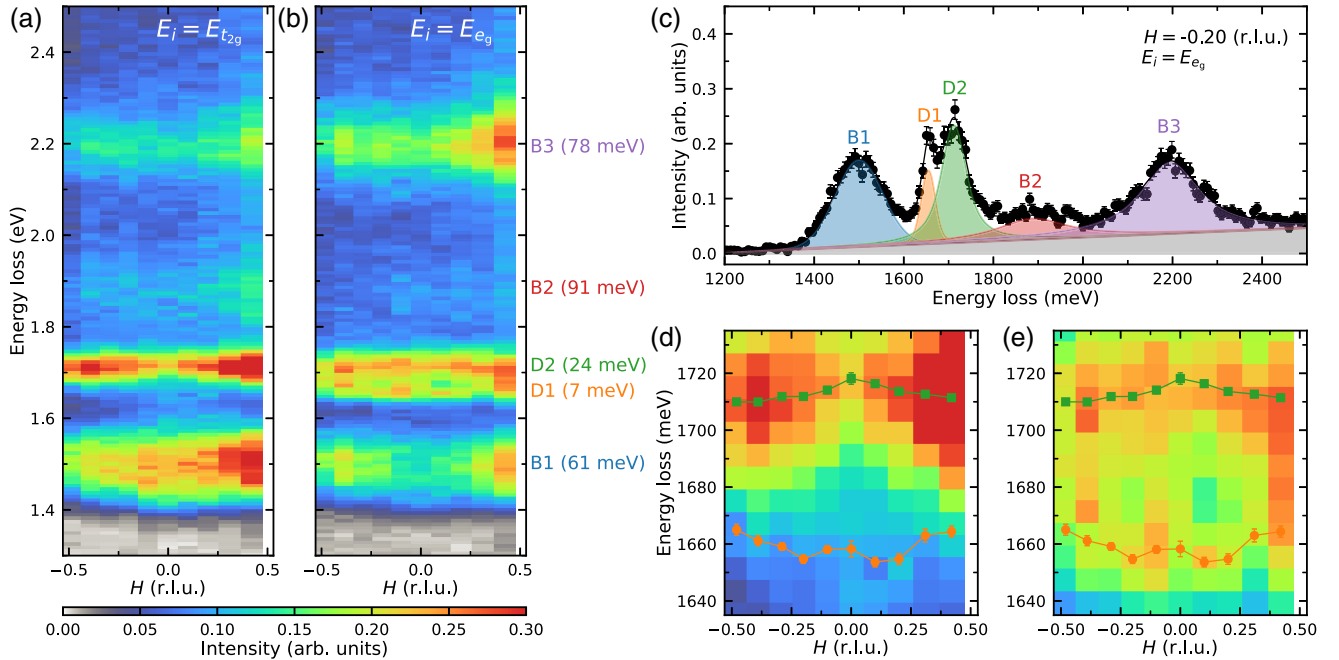

FIG. 2. Dispersion of the dark excitons. (a),(b) RIXS intensity map at $T = 30$ K as a function of in-plane momentum transfer H measured with (a) $E_i = E_{t_{2g}}$, where the D2 exciton is strongest, and (b) $E_i = E_{e_g}$, where the D1 and D2 excitons are visible. The two dark excitons are much narrower than the other bright excitons, as seen by inspecting the intrinsic resolution deconvolved HWHM of the peaks as included in brackets after the peak labels. (c) Representative fit at $H = -0.20$ r.l.u. with $E_i = E_{e_g}$. (d),(e) Enlargement of the dark exciton dispersion at (d) $E_i = E_{t_{2g}}$ and (e) $E_i = E_{e_g}$. For each momentum, we cofit the spectra taken at the two resonances with shared exciton energies and widths. The cofitted energy dispersion overlays the color maps.

V. TEMPERATURE DEPENDENCE

Next, we examine the temperature dependence of RIXS spectra at $E_i = E_{t_{2g}}$ through the FM transition temperature $T_c = 61$ K up to room temperature. Figure 3 plots data and
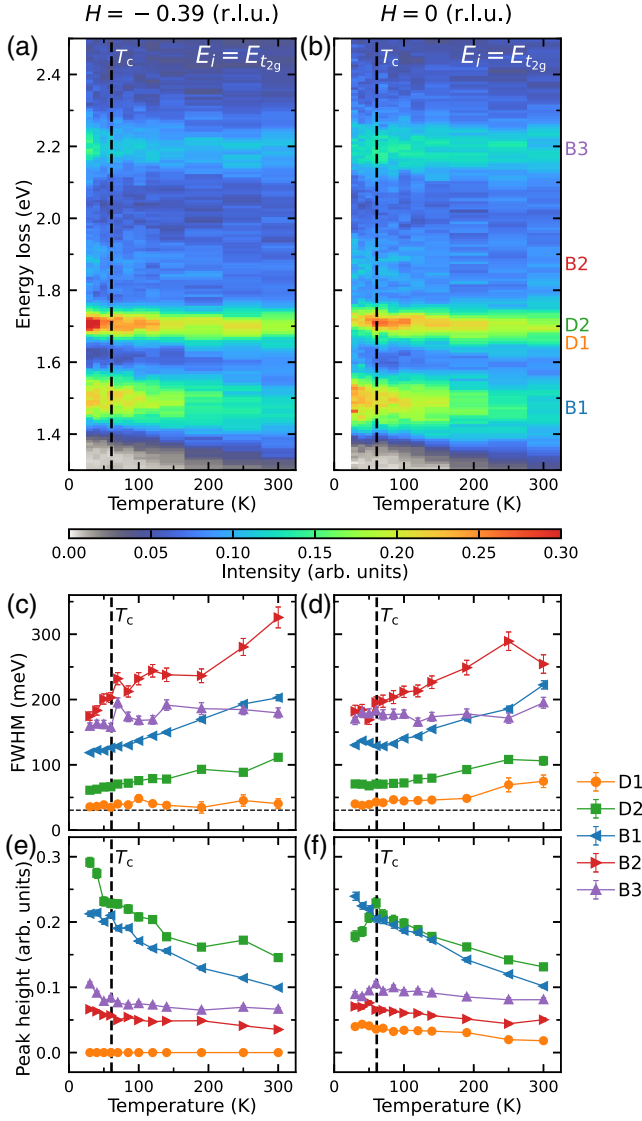

FIG. 3. Temperature dependence of the dark excitons. (a),(b) RIXS intensity map as a function of temperature measured at two different in-plane momenta ($H = -0.39$ and $H = 0$ r.l.u., respectively) with the same incident energy $E_{t_{2g}}$. (c)–(f) Corresponding FWHM and peak height extracted from the fits as a function of the temperature. Changes in peak height through T_c primarily reflect changes in the integrated intensity of the peaks. We plot the peak intensity here because this quantity can be determined more precisely. Error bars represent one standard deviation. The fits are performed by cofitting spectra taken at two incident energies with shared exciton energies and widths for each momentum and temperature. The data taken at the other incident energy E_{e_g} are shown in Supplemental Material Sec. S2 [32]. The vertical black lines indicate the FM transition temperature T_c, and the horizontal black lines in (c) and (d) indicate the energy resolution.

fits at two momenta. All excitons show an overall trend toward larger widths at higher temperatures. Such behavior is similar to RIXS measurements of excitons in other related materials such as NiPS$_3$ [13] and nickel dihalides [17,24]. D2 (and, to a lesser extent, B3) shows a clear anomaly around the FM transition temperature T_c. The trends are even opposite through T_c at the two selected momenta, demonstrating an unusual momentum-dependent coupling between magnetism and dark exciton states. Other bright excitons, such as B1, also exhibit anomalies across T_c at certain momenta and incident energies (see Supplemental Fig. S3 [32]). The momentum dependence of these anomalies indicates underlying physics that cannot be fully captured by established cluster-based methods commonly used to interpret RIXS. We also note that B1 (and, to a lesser extent, D2) softens steadily upon warming, particularly above T_c, which is reminiscence of the exciton behavior in NiPS$_3$ and NiI$_2$ [13,24]. Such interesting behavior might be related to the electron-phonon interactions, which was used to explain the electronic gap shift observed in optics [34].

VI. ELECTRONIC CHARACTER OF EXCITONS

An advantage of RIXS compared to optics is that it couples directly to dipole-forbidden transitions in a well-known way, allowing us to extract the electronic character of the excitons. Indeed, ambiguities in the optical cross section for these excitons have led to different suggestions for the types of excitations present in chromium trihalides in the 1.50–1.85 eV window including features coming from trigonal crystal fields to vibronic structures [21,22]. To interpret the present spectra, we built an Anderson impurity model (AIM) for CrI$_3$ and computed the RIXS spectrum using ED methods [35]. The model includes Coulomb repulsion, Hund's coupling, crystal field, and hopping terms derived from the Wannierization of our CrI$_3$ density functional theory (DFT) calculations as detailed in the Appendix. The spectra, shown in Figs. 4(a) and 4(b), capture the exciton energies including the double-peak structure of the two dark excitons and the overall trends in the resonances.

To identify the excitons, we report the final state expectation values of the spin-squared $\langle \hat{S}^2 \rangle$ and electron population operators in Figs. 4(c)–4(e). We note that it is vital to have a small charge-transfer energy (in fact, the best fit is achieved using $\Delta = -1.3$ eV with an error bar of approximately 1 eV) to obtain the correct energies for the entire spectrum. Such a small (or even slightly negative) charge-transfer energy leads to approximately four electrons in the d states and approximately one hole occupying the ligand e_g orbitals not only in the ground states, but also in the low-energy excitations, as shown in Fig. 4(e), and in accordance with previous DFT-based results [31,36–38]. The importance of charge transfer is further underlined by the fact that a single-site atomic model cannot adequately
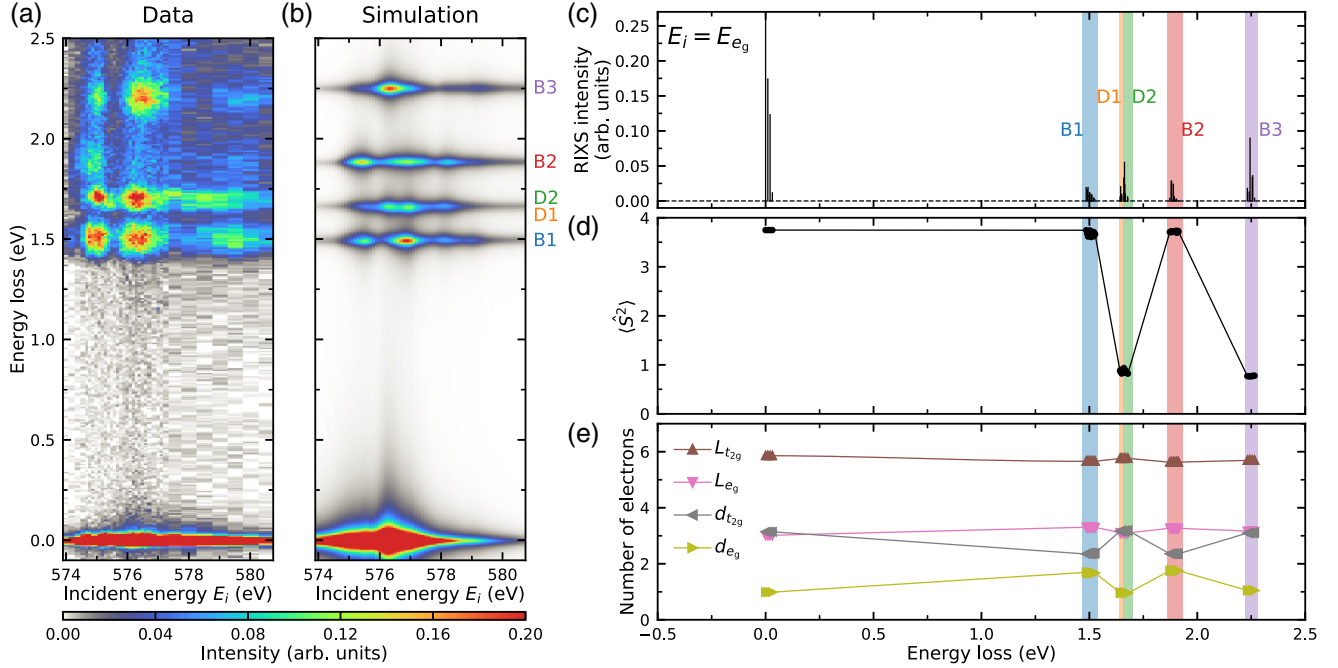
FIG. 4. Electronic character of the dark excitons. (a) RIXS intensity map as a function of incident photon energy through the Cr L_3 resonance. These are the same data presented in Fig. 1 with an energy window chosen to highlight the low-energy excitations. (b) RIXS calculations that reproduce the energy and resonant profile of the five lowest-energy excitons in the material. (c) Calculated RIXS stick diagram at the main resonant energy E_{e_g}. (d),(e) Analysis of the ground and excited states for the calculated RIXS spectrum. (d) Expectation value of the total spin operator squared $\langle \hat{S}^2 \rangle$. (e) Electron occupations of Cr $3d$ (denoted by d) and ligand (denoted by L) orbitals.

fit the spectrum (see Supplemental Material Sec. 5A [32]). As such, the excitations observed here have substantial I character and are not strictly dd excitations. The non-dispersive modes observed here are well described by the broader concept of ligand-field excitons [39]. However, since these are by definition local, the dispersive D1 and D2 are, in our opinion, best termed as excitons, although all these terms share some similarities [40].

The ground state features half-filled t_{2g} orbitals, with $\langle \hat{S}^2 \rangle \approx 3.75$, corresponding to a high-spin configuration with $S = 3/2$. The D1 and D2 dark excitons involve only a small change in electron population, with the largest component of charge motion being about 0.1 electrons moving from the ligand $L_{t_{2g}}$ to the L_{e_g} states; the change from d to L states is even smaller at 0.03 electrons. More notably, this transition involves a low-spin configuration final state close to $S = 1/2$. Consequently, the energy scale of these dark excitons is determined mainly by the Hund's coupling for Cr $3d$ orbitals, consistent with their spin-flip character. Although D1 and D2 have dominant t_{2g} character, they feature nonzero mixing with the e_g manifold [see Fig. 4(e)]. This mixing endows D1 and D2 with a distinct orbital angular momentum, leading to their small energetic splitting and their distinct resonant profile at the t_{2g} and e_g conditions. The nearby bright excitons B1 and B2 are both crystal field transitions, conserving spin and moving an

electron from the t_{2g} to the e_g states. Their energies are determined primarily by a combination of crystal field $10D_q$ and charge-transfer energy Δ (see the Appendix for the definitions of these quantities).

The higher-energy B3 exciton is again a spin-flip transition but with different symmetry that also redistributes a small amount of weight from the t_{2g} to e_g states. Its intensity exhibits a temperature dependence similar to that of the dark exciton D2 (although the change is less dramatic) in Figs. 3(e) and 3(f), possibly implying their similar spin-flip character. B3 is particularly broad, suggesting that this mode may be coupling to other excitations. Such a coupling could play a role in the finite optical cross section for this mode, which is larger than expected since it is a spin-flip transition. It is also possible that extended lattice models could be required to understand the detailed nature of the B2 and B3 excitons and their optical cross section more fully, as suggested by many-body perturbation theory plus Bethe-Salpeter equation calculations [31,41].

VII. DISCUSSION AND CONCLUSIONS

The results here provide the first example of dispersive excitons in a FM vdW material, extending the recent identification of this phenomenon in antiferromagnetic vdW materials such as NiPS$_3$ [15] and nickel dihalides [17]. These dispersive excitons are all sharp spin-flip

excitations bound by Hund's exchange interactions. The sharpness of the exciton (i.e., its long lifetime) may be related to its spin-flip nature, because such transitions do not involve charge redistribution and, therefore, have minimal couplings to phonons and reduced efficiency of radiative recombination [20]. Prior works have made similar arguments for $NiPS_3$ and NiI_2, where the spin-flip character of excitons is regarded as the major aspect of their physics [13,15,42]. The small electron transfer involved in the transition has been suggested to play a minor role, even though the magnitude of electron transfer in $NiPS_3$ is of the order of 0.2 electrons and about 7 times larger than the charge transfer observed here [15].

All these excitons also have appreciable ligand-hole involvement due to the small charge-transfer energy, which may facilitate exciton propagation in the magnetic background [17]. However, there are also key distinctions between CrI_3 excitons and their counterparts in antiferromagnets. One clear difference is the exciton bandwidth. Phenomenologically, unlike the case in $NiPS_3$ or nickel dihalides where the exciton bandwidth is significantly smaller than the magnon bandwidth [15,17], both dark excitons in CrI_3 have bandwidths comparable to the magnon bands [33]. In addition, these excitons exhibit a peculiar temperature dependence clearly correlated with T_c. Since CrI_3 exhibits layer-dependent magnetism [19], it would be of high interest to examine the exciton behaviors in the few-layer limit of CrI_3 in the near future. We also note that the energies of the CrI_3 dark excitons are higher than the electronic band gap, which was reported to be 1.1–1.3 eV [34] in CrI_3. This above-band-gap character may explain relatively large linewidth and their darkness in optics due to the strong sloping background coming from interband transitions. As a comparison, the previously discovered spin-flip excitons in $NiPS_3$ involve below-band-gap transitions [13,15,43].

In conclusion, we report two dark excitons in CrI_3 directly measured with high-resolution RIXS. Our results showcase RIXS as a powerful tool in studying these dark states with a readily interpretable cross section and large momentum space coverage, complementary to optical measurements. The excitons feature strong coupling with the magnetism—they disperse with bandwidths similar to magnons and display unusual temperature dependence across the magnetic transition temperature. Our results will guide future optical experiments to detect and manipulate these dark excitons in CrI_3. In the past, various methods have been employed to brighten dark excitons in optical measurements, such as the application of an in-plane magnetic field [3], near-field coupling to surface plasmon polaritons [44], or by nano-optical tip-enhanced approaches [45]. With the better-targeted energies provided by our study, there is a high likelihood of probing these dark excitons in CrI_3 using these advanced optical techniques. Indeed, the possibility of accessing D1 and/or D2 optically is supported by a subset of the prior optical studies, which identified shoulder features

in the spectra indicative of modes in the 1.7 eV range [20]. Moreover, our ED calculations will also inform future theory in more accurately describing the electronic properties of CrI_3. We believe that our discovery of dark excitons in CrI_3 is just the tip of the iceberg, and the utilization of RIXS will expedite the expansion of this family of materials and foster both the understanding of the fundamental physics and the potential applications of dark excitons in devices.

Note added in proof. Recently, we became aware of another spectroscopic study of CrI_3, whose high-resolution RIXS results and conclusions are in good accordance with those we present here [46].

DATA AVAILABILITY

The supporting data for the plots in this article are openly available from the Zenodo database [47].

APPENDIX: EDRIXS CALCULATIONS

The RIXS spectra in this work were simulated based on standard ED methods implemented in the open source software EDRIXS [35]. The RIXS cross section was calculated using the Kramers-Heisenberg formula with the polarization-dependent dipole approximation. The model we employ here is an AIM, which was constructed using the bonding ligand orbitals of a CrI_6 cluster model.

Here, we provide details on the parameters that we used and the methods that we employed to determine them.

In an AIM, we can represent a cluster with fewer orbitals by using symmetry-adapted linear combinations of ligand orbitals [48], making the calculation numerically much more efficient with essentially no loss of accuracy. In our case, we have ten Cr $3d$ spin orbitals and ten ligand spin orbitals with the same symmetry, so there are 13 electrons in total occupying 20 spin-resolved orbitals in the initial and final states. In the intermediate states, the Cr $2p$ orbitals are included to simulate the core hole created in the RIXS process. The calculations were performed in the full basis using the FORTRAN ED solver provided in EDRIXS [35]. For the RIXS cross section calculations, we have the experimental geometry explicitly considered; i.e., the scattering angle 2Θ is fixed to 150°, and the sample angle θ is kept at 14.5°. An inverse core-hole lifetime $\Gamma_c = 0.3$ eV HWHM was used to fit the observed width of the resonance, and the final state energy loss spectra were broadened using a Lorentzian function with a FWHM of 0.03 eV, in order to match the observed minimum width of the dark excitons.

The Hamiltonian of the model includes the Coulomb interactions, on-site energy for each orbital, hoppings between different orbitals, spin-orbit coupling, and the Zeeman interaction.

We parametrize the Coulomb interactions via Slater integrals, which include F_{dd}^0, F_{dd}^2, and F_{dd}^4 for the Cr $3d$ orbitals and F_{dp}^0, F_{dp}^2, G_{dp}^1, and G_{dp}^3 for the interactions between Cr $3d$ and $2p$ core orbitals in the intermediate states. F_{dd}^0 and F_{dp}^0 are related to the Cr $3d$ on-site

Coulomb repulsion U_{dd} and core-hole potential U_{dp}, respectively, which are discussed later. The rest of the parameters are obtained by starting from their Hartree-Fock atomic values and scaling them down to account for the screening effect in the solids. For simplicity, we used two overall scaling factors: one for Cr $3d$ orbitals (k_{dd}) and the other for the core-hole interactions (k_{dp}).

Hopping integrals describe hybridization between different orbitals. This can be expressed using a 10×10 matrix H_{hopping}. We determined the off-diagonal interorbital hopping parameters from first principles by calculating the electronic structure with the VASP DFT code [49,50]. In this case, we used the Perdew-Burke-Ernzerhof generalized gradient approximation [51] for the exchange-correlation functional without spin-orbit coupling. We employed projector augmented wave pseudopotentials [52,53], considering Cr $3p$ electrons as valence (Cr_pv). The energy cutoff was set to 350 eV, and we used a $15 \times 15 \times 15$ Monkhorst-Pack k-point mesh. We used a linear mixing parameter AMIX of 0.05 and a smearing parameter SIGMA of 0.05 eV. Finally, a tight-binding model was constructed using WANNIER90 [54–56]. We performed a Wannier projection of Cr $3d$ and I $5p$ orbitals without maximal localization. Disentanglement was omitted, since these states form a well-isolated band set within the chosen energy window. The band structure from DFT calculations and the Wannier projected bands are shown in Fig. S12 [32]. The ligand orbitals were constructed from the appropriate linear combinations of the Wannier orbitals [47]. The hopping terms we obtained from this method are listed below (in units of eV):

$$H_{\text{hopping}} = $$

	$d_{3z^2-r^2}$	d_{xz}	d_{yz}	$d_{x^2-y^2}$	d_{xy}	$L_{3z^2-r^2}$	L_{xz}	L_{yz}	$L_{x^2-y^2}$	L_{xy}
$d_{3z^2-r^2}$	−9.634	0.002	0.001	0	−0.003	−2.008	−0.011	−0.019	−0.001	0.03
d_{xz}	0.002	−10.244	0.003	0.003	0.003	−0.001	−1.272	−0.001	0.007	−0.002
d_{yz}	0.001	0.003	−10.244	−0.003	0.003	0.006	−0.002	−1.272	−0.002	−0.001
$d_{x^2-y^2}$	0.0	0.003	−0.003	−9.634	0	0.001	−0.028	0.024	−2.008	0.004
d_{xy}	−0.003	0.003	0.003	0	−10.244	0.005	−0.001	−0.002	−0.004	−1.272
$L_{3z^2-r^2}$	−2.008	−0.001	0.006	0.001	−0.005	2.689	0.01	0.015	0.0	−0.026
L_{xz}	−0.011	−1.272	−0.002	−0.028	−0.001	0.01	1.208	−0.017	0.024	−0.017
L_{yz}	−0.019	−0.001	−1.272	0.024	−0.002	0.015	−0.017	1.208	−0.021	−0.017
$L_{x^2-y^2}$	−0.001	0.007	−0.002	−2.008	−0.004	0.0	0.024	−0.021	2.689	−0.003
L_{xy}	0.03	−0.002	−0.001	0.004	−1.272	−0.026	−0.017	−0.017	−0.003	1.208

$$\text{(A1)}$$

Since hopping depends on how electronic wave functions are spread between different atoms, it is only weakly influenced by strongly correlated physics, and DFT generally captures the magnitude of hopping quite accurately.

For this reason, we consider the off-diagonal interorbital hopping values fixed to the quoted DFT-derived values. The on-site energies correspond to the diagonal elements in the hopping matrix H_{hopping} above. These on-site energies

TABLE I.   Full list of parameters used in the AIM calculations [except for the hopping integrals, which are provided in Eq. (A1)]. $F_{dd,\text{i}}$ and $F_{dd,\text{n}}$ are for the initial and intermediate states, respectively. Units are eV.

$10D_q$	$10D_q^L$	Δ	U_{dd}	U_{dp}	$F_{dd,\text{i}}^2$	$F_{dd,\text{i}}^4$	$F_{dd,\text{n}}^2$	$F_{dd,\text{n}}^4$	F_{dp}^2	G_{dp}^1	G_{dp}^3	ζ_i	ζ_n	ζ_c
0.61	1.481	−1.3	4.0	6.0	7.005	4.391	7.537	4.726	3.263	2.394	1.361	0.035	0.047	5.667

for the Cr $3d$ states are not easily obtainable from first principles because of the effects of strong correlations and the challenges in handling double-counting effects. We, therefore, consider the Cr $3d$ crystal field as a fitting parameter, which, in view of the approximately cubic symmetry of the Cr coordination, is specified by $10D_q$, which represents the splitting between the t_{2g} and e_g orbitals.

Since Coulomb interactions in the I $5p$ states are relatively weak and since the probability that these states are occupied by multiple holes is relatively low, the crystal field on the states is more accurately captured by DFT, so, to reduce the number of fitting parameters, we fix the ligand orbital crystal field $10D_q^L$ to the value extracted from our DFT results (1.481 eV). In this work, we define the charge-transfer, Δ, and Coulomb repulsion, U_{dd}, energies as the energy cost of specific transitions in the material with the Cr-ligand hopping switched off. U_{dd} reflects a $d_i^3 d_j^3 \rightarrow d_i^2 d_j^4$ transition, and Δ is defined as the energy for a $d_i^3 \rightarrow d_i^4 \underline{L}$ transition, where i and j label Cr sites and $\underline{L}$ denotes an iodine ligand hole. These energies include the effect of the Cr crystal field and represent the energies for a transition into the lowest-energy *ligand* orbital (rather than the center of the I p states). From a practical point of view, we perform our calculations varying the energy splitting of the Cr and ligand states, and we subsequently determine Δ by diagonalizing the isolated Cr and ligand configurations and computing the appropriate differences in energy. The values of the diagonal elements in Eq. (A1) are the final on-site energies determined for our model.

In the intermediate states with the presence of a core hole, we include a core-hole potential U_{dp}. U_{dd} is usually 4–6 eV in early transition metals, and it is usually smaller when the charge transfer energy is small (which we see is the case here), so we choose 4 eV [57,58]. U_{dp} is only weakly dependent on solid state effects, so we choose a typical value of 6 eV.

The spin-orbit coupling terms for the Cr $3d$ orbitals (ζ_i and ζ_n for the initial and intermediate states, respectively) are weak and have negligible effects on the spectra. We consequently simply fixed them to their atomic values. Since we measured the RIXS energy map only at the L_3 edge, we also simply fixed the core-hole spin-orbit coupling parameter ζ_c to its atomic value.

A small Zeeman interaction term $g\mu_B \mathbf{B} \cdot \mathbf{S}$ was applied to the total spin angular momentum of the system, serving as the effective exchange field in the magnetically ordered

state. We fixed $\mu_B B = 0.005$ eV to match the energy scale of the exchange interactions in CrI$_3$ [33].

In summary, we have four free parameters in our model, i.e., k_{dd}, k_{dp}, $10D_q$, and Δ. Most of these values are constrained by physical considerations. k_{dd} and k_{dp} quantify the screening. These are known to vary within a range of 0.5–0.9 from prior studies, and these values typically also have reasonably similar values since both are affected by similar screening processes [59]. $10D_q$ in $3d$ octahedrally coordinated transition metal material ranges from about 0.5 to 3 eV, and, since iodine is relatively large size in ionic radius and relativity weakly electronegative, we expect a value in the lower half of this range. k_{dd}, k_{dp}, $10D_q$, and Δ have distinct effects on the RIXS energy map. k_{dd} directly scales the Hund's coupling and, hence, controls the energies of the dark excitons D1 and D2. The energies of the bright excitons B1 and B2 are primarily determined by both $10D_q$ and Δ. k_{dp} mainly affects the resonance profiles of these peaks. Thanks to the richly detailed spectra, the finite physically reasonable range of parameters, and the distinct effects of different parameters, we successfully obtained a well-constrained model with final parameters as $k_{dd} = 0.65$, $k_{dp} = 0.5$, $10D_q = 0.61$ eV, and $\Delta = -1.3$ eV and verified that no other solutions exist. The level of agreement compares favorably with what can be expected for a model of this type accurately capturing the energy of the excitations while roughly capturing trends in peak intensities [13,15,17,24]. The full list of parameters used in the model is shown in Table I. The estimated error bars are approximately 1 eV for all the Coulomb interactions and the charge-transfer energy Δ and approximately 0.2 eV for $10D_q$.

———

[1] S. Koch, M. Kira, G. Khitrova, and H. Gibbs, *Semiconductor excitons in new light*, Nat. Mater. **5**, 523 (2006).

[2] W. R. Kitzmann, J. Moll, and K. Heinze, *Spin-flip luminescence*, Photochem. Photobiol. Sci. **21**, 1309 (2022).

[3] X.-X. Zhang, T. Cao, Z. Lu, Y.-C. Lin, F. Zhang, Y. Wang, Z. Li, J. C. Hone, J. A. Robinson, D. Smirnov, S. G. Louie, and T. F. Heinz, *Magnetic brightening and control of dark excitons in monolayer* WSe$_2$, Nat. Nanotechnol. **12**, 883 (2017).

[4] E. Poem, Y. Kodriano, C. Tradonsky, N. H. Lindner, B. D. Gerardot, P. M. Petroff, and D. Gershoni, *Accessing the dark exciton with light*, Nat. Phys. **6**, 993 (2010).

[5] M. Nirmal, D. J. Norris, M. Kuno, M. G. Bawendi, A. L. Efros, and M. Rosen, *Observation of the "dark exciton" in* CdSe *quantum dots*, Phys. Rev. Lett. **75**, 3728 (1995).

[6] D. N. Congreve, J. Lee, N. J. Thompson, E. Hontz, S. R. Yost, P. D. Reusswig, M. E. Bahlke, S. Reineke, T. V. Voorhis, and M. A. Baldo, *External quantum efficiency above 100% in a singlet-exciton-fission–based organic photovoltaic cell*, Science **340**, 334 (2013).

[7] G. Wang, A. Chernikov, M. M. Glazov, T. F. Heinz, X. Marie, T. Amand, and B. Urbaszek, *Colloquium: Excitons in atomically thin transition metal dichalcogenides*, Rev. Mod. Phys. **90**, 021001 (2018).

[8] K. S. Burch, D. Mandrus, and J. G. Park, *Magnetism in two-dimensional van der Waals materials*, Nature (London) **563**, 47 (2018).

[9] C. Gong and X. Zhang, *Two-dimensional magnetic crystals and emergent heterostructure devices*, Science **363**, eaav4450 (2019).

[10] Q. H. Wang *et al.*, *The magnetic genome of two-dimensional van der Waals materials*, ACS Nano **16**, 6960 (2022).

[11] Y. Ahn, X. Guo, S. Son, Z. Sun, and L. Zhao, *Progress and prospects in two-dimensional magnetism of van der Waals materials*, Prog. Quantum Electron. **93**, 100498 (2024).

[12] K. F. Mak, J. Shan, and D. C. Ralph, *Probing and controlling magnetic states in 2D layered magnetic materials*, Nat. Rev. Phys. **1**, 646 (2019).

[13] S. Kang, K. Kim, B. H. Kim, J. Kim, K. I. Sim, J. U. Lee, S. Lee, K. Park, S. Yun, T. Kim, A. Nag, A. Walters, M. Garcia-Fernandez, J. Li, L. Chapon, K. J. Zhou, Y. W. Son, J. H. Kim, H. Cheong, and J. G. Park, *Coherent many-body exciton in van der Waals antiferromagnet* NiPS₃, Nature (London) **583**, 785 (2020).

[14] Y. J. Bae, J. Wang, A. Scheie, J. Xu, D. G. Chica, G. M. Diederich, J. Cenker, M. E. Ziebel, Y. Bai, H. Ren, C. R. Dean, M. Delor, X. Xu, X. Roy, A. D. Kent, and X. Zhu, *Exciton-coupled coherent magnons in a 2D semiconductor*, Nature (London) **609**, 282 (2022).

[15] W. He, Y. Shen, K. Wohlfeld, J. Sears, J. Li, J. Pelliciari, M. Walicki, S. Johnston, E. Baldini, V. Bisogni, M. Mitrano, and M. P. M. Dean, *Magnetically propagating Hund's exciton in van der Waals antiferromagnet* NiPS₃, Nat. Commun. **15**, 3496 (2024).

[16] M. F. DiScala, D. Staros, A. de la Torre, A. Lopez, D. Wong, C. Schulz, M. Barkowiak, V. Bisogni, J. Pelliciari, B. Rubenstein, and K. W. Plumb, *Elucidating the role of dimensionality on the electronic structure of the van der Waals antiferromagnet* NiPS₃, Adv. Phys. Res. **3**, 2300096 (2024).

[17] C. A. Occhialini, Y. Tseng, H. Elnaggar, Q. Song, M. Blei, S. A. Tongay, V. Bisogni, F. M. F. de Groot, J. Pelliciari, and R. Comin, *Nature of excitons and their ligand-mediated delocalization in nickel dihalide charge-transfer insulators*, Phys. Rev. X **14**, 031007 (2024).

[18] N. P. Wilson, W. Yao, J. Shan, and X. Xu, *Excitons and emergent quantum phenomena in stacked 2D semiconductors*, Nature (London) **599**, 383 (2021).

[19] B. Huang, G. Clark, E. Navarro-Moratalla, D. R. Klein, R. Cheng, K. L. Seyler, D. Zhong, E. Schmidgall, M. A. McGuire, D. H. Cobden, W. Yao, D. Xiao, P. Jarillo-Herrero, and X. Xu, *Layer-dependent ferromagnetism in*

a van der Waals crystal down to the monolayer limit, Nature (London) **546**, 270 (2017).

[20] W. Jin, H. H. Kim, Z. Ye, G. Ye, L. Rojas, X. Luo, B. Yang, F. Yin, J. S. A. Horng, S. Tian, Y. Fu, G. Xu, H. Deng, H. Lei, A. W. Tsen, K. Sun, R. He, and L. Zhao, *Observation of the polaronic character of excitons in a two-dimensional semiconducting magnet* CrI₃, Nat. Commun. **11**, 4780 (2020).

[21] I. Pollini and G. Spinolo, *Intrinsic optical properties of* CrCl₃, Phys. Status Solidi (b) **41**, 691 (1970).

[22] V. M. Bermudez and D. S. McClure, *Spectroscopic studies of the two-dimensional magnetic insulators chromium trichloride and chromium tribromide—I*, J. Phys. Chem. Solids **40**, 129 (1979).

[23] K. L. Seyler, D. Zhong, D. R. Klein, S. Gao, X. Zhang, B. Huang, E. Navarro-Moratalla, L. Yang, D. H. Cobden, M. A. McGuire, W. Yao, D. Xiao, P. Jarillo-Herrero, and X. Xu, *Ligand-field helical luminescence in a 2D ferromagnetic insulator*, Nat. Phys. **14**, 277 (2018).

[24] S. Son, Y. Lee, J. H. Kim, B. H. Kim, C. Kim, W. Na, H. Ju, S. Park, A. Nag, K.-J. Zhou, Y.-W. Son, H. Kim, W.-S. Noh, J.-H. Park, J. S. Lee, H. Cheong, J. H. Kim, and J.-G. Park, *Multiferroic-enabled magnetic-excitons in 2d quantum-entangled van der Waals antiferromagnet* NiI₂, Adv. Mater. **34**, 2109144 (2022).

[25] M. Mitrano, S. Johnston, Y.-J. Kim, and M. P. M. Dean, *Exploring quantum materials with resonant inelastic x-ray scattering*, Phys. Rev. X **14**, 040501 (2024).

[26] M. A. McGuire, H. Dixit, V. R. Cooper, and B. C. Sales, *Coupling of crystal structure and magnetism in the layered, ferromagnetic insulator* CrI₃, Chem. Mater. **27**, 612 (2015).

[27] H. Miao, J. Lorenzana, G. Seibold, Y. Y. Peng, A. Amorese, F. Yakhou-Harris, K. Kummer, N. B. Brookes, R. M. Konik, V. Thampy, G. D. Gu, G. Ghiringhelli, L. Braicovich, and M. P. M. Dean, *High-temperature charge density wave correlations in* La₁.₈₇₅Ba₀.₁₂₅CuO₄ *without spin–charge locking*, Proc. Natl. Acad. Sci. U.S.A. **114**, 12430 (2017).

[28] L. J. P. Ament, M. Van Veenendaal, T. P. Devereaux, J. P. Hill, and J. Van Den Brink, *Resonant inelastic x-ray scattering studies of elementary excitations*, Rev. Mod. Phys. **83**, 705 (2011).

[29] A. Ghosh, H. J. Jönsson, D. J. Mukkattukavil, Y. Kvashnin, D. Phuyal, P. Thunström, M. Agåker, A. Nicolaou, M. Jonak, R. Klingeler, M. V. Kamalakar, T. Sarkar, A. N. Vasiliev, S. M. Butorin, O. Eriksson, and M. Abdel-Hafiez, *Magnetic circular dichroism in the dd excitation in the van der Waals magnet* CrI₃ *probed by resonant inelastic x-ray scattering*, Phys. Rev. B **107**, 115148 (2023).

[30] Y. C. Shao, B. Karki, W. Huang, X. Feng, G. Sumanasekera, J.-H. Guo, Y.-D. Chuang, and B. Freelon, *Spectroscopic determination of key energy scales for the base Hamiltonian of chromium trihalides*, J. Phys. Chem. Lett. **12**, 724 (2021).

[31] M. Wu, Z. Li, T. Cao, and S. G. Louie, *Physical origin of giant excitonic and magneto-optical responses in two-dimensional ferromagnetic insulators*, Nat. Commun. **10**, 2371 (2019).

[32] See Supplemental Material at http://link.aps.org/supplemental/10.1103/PhysRevX.15.011042 for further details of the calculations and fittings.

[33] L. Chen, J.-H. Chung, B. Gao, T. Chen, M. B. Stone, A. I. Kolesnikov, Q. Huang, and P. Dai, *Topological spin excitations in honeycomb ferromagnet* CrI_3, Phys. Rev. X **8**, 041028 (2018).

[34] L. Tomarchio, S. Macis, L. Mosesso, L. T. Nguyen, A. Grilli, M. C. Guidi, R. J. Cava, and S. Lupi, *Low energy electrodynamics of* CrI_3 *layered ferromagnet*, Sci. Rep. **11**, 23405 (2021).

[35] Y. L. Wang, G. Fabbris, M. P. Dean, and G. Kotliar, *EDRIXS: An open source toolkit for simulating spectra of resonant inelastic x-ray scattering*, Comput. Phys. Commun. **243**, 151 (2019).

[36] I. V. Kashin, V. V. Mazurenko, M. I. Katsnelson, and A. N. Rudenko, *Orbitally-resolved ferromagnetism of monolayer* CrI_3, 2D Mater. **7**, 025036 (2020).

[37] S. Acharya, D. Pashov, B. Cunningham, A. N. Rudenko, M. Rösner, M. Grüning, M. Van Schilfgaarde, and M. I. Katsnelson, *Electronic structure of chromium trihalides beyond density functional theory*, Phys. Rev. B **104**, 155109 (2021).

[38] Y. O. Kvashnin, A. N. Rudenko, P. Thunström, M. Rösner, and M. I. Katsnelson, *Dynamical correlations in single-layer* CrI_3, Phys. Rev. B **105**, 205124 (2022).

[39] C. J. Ballhausen, *Introduction to Ligand Field Theory* (McGraw-Hill, New York, 1962).

[40] See Supplemental Material Sec. S6 [32] for more discussion of this issue.

[41] S. Acharya, D. Pashov, A. N. Rudenko, M. Rösner, M. v. Schilfgaarde, and M. I. Katsnelson, *Real- and momentum-space description of the excitons in bulk and monolayer chromium tri-halides*, npj 2D Mater. Appl. **6**, 1 (2022).

[42] I. J. Hamad, C. S. Helman, L. O. Manuel, A. E. Feiguin, and A. A. Aligia, *Singlet polaron theory of low-energy optical excitations in* $nips_3$, Phys. Rev. Lett. **133**, 146502 (2024).

[43] S. Y. Kim, T. Y. Kim, L. J. Sandilands, S. Sinn, M. C. Lee, J. Son, S. Lee, K. Y. Choi, W. Kim, B. G. Park, C. Jeon, H. D. Kim, C. H. Park, J. G. Park, S. J. Moon, and T. W. Noh, *Charge-spin correlation in van der Waals antiferromagnet* $NiPS_3$, Phys. Rev. Lett. **120**, 136402 (2018).

[44] Y. Zhou, G. Scuri, D. S. Wild, A. A. High, A. Dibos, L. A. Jauregui, C. Shu, K. De Greve, K. Pistunova, A. Y. Joe, T. Taniguchi, K. Watanabe, P. Kim, M. D. Lukin, and H. Park, *Probing dark excitons in atomically thin semiconductors via near-field coupling to surface plasmon polaritons*, Nat. Nanotechnol. **12**, 856 (2017).

[45] K.-D. Park, T. Jiang, G. Clark, X. Xu, and M. B. Raschke, *Radiative control of dark excitons at room temperature by* *nano-optical antenna-tip Purcell effect*, Nat. Nanotechnol. **13**, 59 (2018).

[46] C. A. Occhialini, L. Nessi, L. G. P. Martins, A. Kemal Demir, Q. Song, V. Hasse, C. Shekhar, C. Felser, K. Watanabe, T. Taniguchi, V. Bisogni, J. Pelliciari, and R. Comin, *Spin-forbidden excitations in the magneto-optical spectra of* CrI_3 *tuned by covalency*, arXiv:2501.17417.

[47] W. He, J. Sears, F. Barantani, T. Kim, J. W. Villanova, T. Berlijn, M. Lajer, M. A. McGuire, J. Pelliciari, V. Bisogni, S. Johnston, E. Baldini, M. Mitrano, and M. P. M. Dean, *Repository for: Dispersive dark excitons in van der Waals ferromagnet* CrI_3, Zenodo, 10.5281/zenodo.14726817.

[48] M. W. Haverkort, M. Zwierzycki, and O. K. Andersen, *Multiplet ligand-field theory using Wannier orbitals*, Phys. Rev. B **85**, 165113 (2012).

[49] G. Kresse and J. Furthmüller, *Efficient iterative schemes for ab initio total-energy calculations using a plane-wave basis set*, Phys. Rev. B **54**, 11169 (1996).

[50] G. Kresse and J. Furthmüller, *Efficiency of ab-initio total energy calculations for metals and semiconductors using a plane-wave basis set*, Comput. Mater. Sci. **6**, 15 (1996).

[51] J. P. Perdew, K. Burke, and M. Ernzerhof, *Generalized gradient approximation made simple*, Phys. Rev. Lett. **77**, 3865 (1996).

[52] P. E. Blöchl, *Projector augmented-wave method*, Phys. Rev. B **50**, 17953 (1994).

[53] G. Kresse and D. Joubert, *From ultrasoft pseudopotentials to the projector augmented-wave method*, Phys. Rev. B **59**, 1758 (1999).

[54] A. A. Mostofi, J. R. Yates, G. Pizzi, Y.-S. Lee, I. Souza, D. Vanderbilt, and N. Marzari, *An updated version of WANNIER90: A tool for obtaining maximally-localised Wannier functions*, Comput. Phys. Commun. **185**, 2309 (2014).

[55] N. Marzari and D. Vanderbilt, *Maximally localized generalized Wannier functions for composite energy bands*, Phys. Rev. B **56**, 12847 (1997).

[56] I. Souza, N. Marzari, and D. Vanderbilt, *Maximally localized Wannier functions for entangled energy bands*, Phys. Rev. B **65**, 035109 (2001).

[57] A. Bocquet, T. Saitoh, T. Mizokawa, and A. Fujimori, *Systematics in the electronic structure of 3d transition-metal compounds*, Solid State Commun. **83**, 11 (1992).

[58] S. Feldkemper and W. Weber, *Generalized calculation of magnetic coupling constants for Mott-Hubbard insulators: Application to ferromagnetic* Cr *compounds*, Phys. Rev. B **57**, 7755 (1998).

[59] F. De Groot and A. Kotani, *Core Level Spectroscopy of Solids* (CRC Press, Boca Raton, 2008).